Vector Magnetic Field Sensors: Operating Principles, Calibration, and Applications

Neoclis Hadjigeorgiou, *Graduate Student Member, IEEE*,
Konstantinos Asimakopoulos, *Graduate Student Member, IEEE*,
Konstantinos Papafotis, *Graduate Student Member, IEEE*, and Paul P. Sotiriadis, *Senior Member, IEEE*

***Abstract*—This review paper explores the most common technologies of vector magnetic field sensors. Specifically, the AMR, GMR, TMR, GMI, Hall, Fluxgate, Search Coil and SQUID sensors are considered. The physical phenomena that permit their operation as well as the structure and operating principles of each sensor are presented. In addition, the basic linear, time-invariant error sources of magnetic sensors are described along with some popular calibration techniques. Finally, some representative application examples of each sensor are described.**

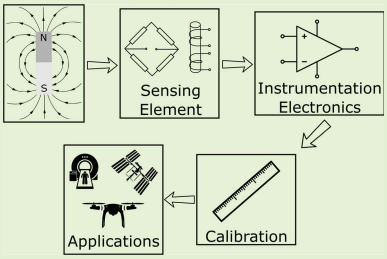

***Index Terms*—AMR, calibration, fluxgate, GMI, GMR, hall effect, magnetic sensors, magnetic shielding, magnetometer.**

I. Introduction

A MAGNETIC field sensor (magnetometer) is a device that measures the magnitude, the direction, or the relative change of the magnetic field. The earliest rudimentary magnetic field sensor is the compass, used for determining the direction of the Earth's magnetic field [1]–[4]. It may be said that the first magnetometer was invented by Carl Friedrich Gauss in 1833, for the measurement of absolute magnetic intensity [3]–[7]. It consisted of a permanent bar magnet suspended horizontally by a gold fiber. Gauss used it to determine the magnitude of the Earth's magnetic field. Along with Wilhelm Eduard Weber, they continued developing the magnetometer, further improving it until the late 1840s.

Except from Gauss and Weber, several other scientists developed novel magnetic field sensors during the 19th century. However, the technology of magnetometers radically changed at the beginning of the 20th century when the electrical current through certain coil structures was used to determine the properties of the local magnetic field [3]–[14]. This new approach enabled the development of more accurate magnetic field sensors while it significantly reduced the measurement time. The advancement of materials science from mid-20th century onwards led to very accurate, miniature-size magnetometers which are today considered key components of several systems [8]–[12], [15].

Manuscript received November 9, 2020; accepted November 23, 2020. Date of publication December 17, 2020; date of current version May 28, 2021. The associate editor coordinating the review of this article and approving it for publication was Dr. Jurgen Kosel. *(Corresponding author: Konstantinos Papafotis.)*

The authors are with the Department of Electrical and Computer Engineering, National Technical University of Athens, 15780 Athens, Greece (e-mail: k.papafotis@gmail.com).

Digital Object Identifier 10.1109/JSEN.2020.3045660

Magnetometer applications range from low-cost commercial devices to high-end industrial, marine, aerospace and military applications. They are used to measure the earth's magnetic field in geophysical surveys, allowing mapping of underground structures and mineral deposits. In navigation, magnetometer's data are exploited for attitude determination by measuring the earth's field direction. They are used in archaeology for locating underground objects and buried sites, in the oil and gas industry for field surveys and in space exploration [5], [9], [15]–[17], [18]–[20], [21]–[23] and in many other fields.

There are two main categories of magnetic field sensors: the scalar ones measuring only the magnitude of the field and the vector ones measuring both the magnitude and the direction of the field. This work focuses on vector magnetic field sensors.

Vector magnetic field sensors are categorized primarily based on their sensing principle, which directly impacts their performance characteristics like measurement range, resolution, frequency response, working temperature and manufacturing cost. They can also be grouped based on other criteria such as the sensed field strength, their noise characteristics and their power consumption [8]–[12], [15], [24]–[26]. The most popular magnetic field sensor technologies used today are the following:

- Search Coils are based on the Induction Law.
- Fluxgates are based on the Induction Law and the ferromagnetic core's properties.
- Hall sensors are based on the Hall effect which is directly related with the Lorentz Force.
- Anisotropic Magneto Resistor (AMR), Giant Magneto Resistor (GMR), Tunneling Magnetoresistor (TMR) and Giant Magneto Impedance (GMI) sensors are based on

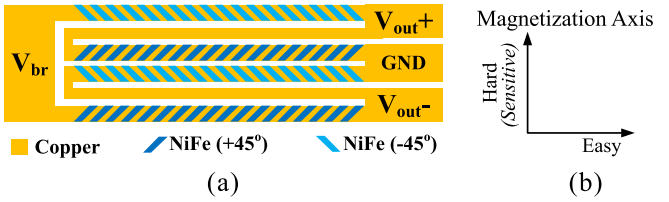

Fig. 1. (a) Typical structure of an AMR magnetometer sensing element and (b) its magnetization axes [27].

the change of the electrical properties of the sensor material when an external magnetic field is applied.

- Superconducting Quantum Interference Device (SQUID) sensors are based on the Josephson Effect and the Aharonov–Bohm effect.

This review paper aims to summarize the physical operating principles and the technologies of magnetic field sensors, their calibration techniques and the range of their applications.

II. Magnetic Sensor Technologies

This section discusses the most common magnetic field sensors and the physical phenomena governing their operation.

A. Anisotropic Magneto-Resistance Sensors (AMR)

Magnetoresistance is the property of certain materials (often ferromagnetic) that their electrical resistance depends on the external magnetic field. It was first discovered by William Thompson (Lord Kelvin) in 1856 [8], [9], [12], [15]. While experimenting with pieces of metals (iron and nickel), he observed that the resistivity of the metal changes according to the angle between the electrical current and the magnetic field. This property is called anisotropic magnetoresistance and it belongs to the category of magneto-transport effects. It implies that the internal structure of the sensing element changes due to rotation of the magnetic domains under the influence of the magnetic field [8]–[12], [15].

A popular ferromagnetic material with such a property is the Ni-Fe permalloy. To further increase its resistance sensitivity to magnetic fields, the sensing element is split into smaller sections interspersed with aluminum or copper [9], [11], [12], [28]. The sensing element is typically built into very thin two-dimensional structures, implying that the element has two magnetization axes: the easy axis and the hard axis.

Magnetoresistance has an even function behavior with respect to the polarity of the magnetic field and so a single magnetoresistor does not suffice to determine the field's polarity. To overcome this drawback, AMR magnetometers are typically formed of four magnetoresistors (sensing elements) in a Wheatstone-bridge configuration. The magnetoresistors, manufactured with a thin-film Ni-Fe permalloy, are composed of several small sections. Consecutive magnetoresistors in the bridge have their small sections axes oriented in opposite, ±45°, angles. This structure is illustrated in Figure 1 along with the easy and hard (sensing) magnetization axes of the bridge and it provides differential sensing capability, [9], [11], [12], [21], [28], [29].

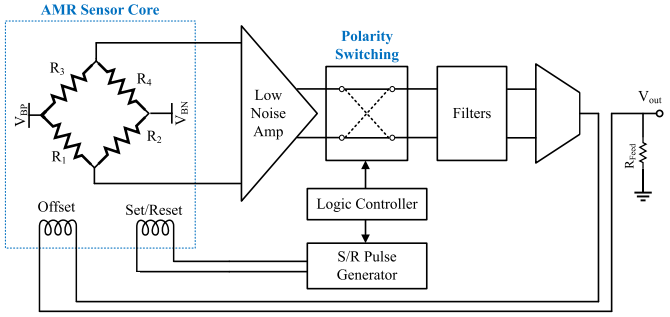

Fig. 2. Example of architecture for AMR sensor with improved performance, including set-reset and offset coils [31].

AMR sensors can be massively fabricated on a chip scale. They are popular and widely used as they are able to measure magnetic fields of low intensity, like the earth's magnetic field. Like every other magnetic field sensor, they also have several drawbacks such as offset, hysteresis, crossfield sensitivity, axes misalignment etc.

To improve performance, some AMR sensors are packaged with two extra coils; the Set-Reset and the Offset one, inductively coupled to the soft and the hard magnetization axes of the sensing element respectively, as shown in Figure 2 [9], [12], [28], [29]. The coils are used to alleviate non-idealities of the sensing element (offset, hysteresis, crossfield sensitivity etc.) [9], [12], [24], [28]–[30].

The set-reset coil is used to (periodically) polarize the sensing element. This is important because the sensing element can be depolarized (e.g. in the present of strong external field or high temperature) leading to degradation of the sensor's performance [9], [12], [28]–[30]. Applying a current to the set-reset coil generates magnetic field on the easy magnetization axis of the ferromagnetic material re-polarizing its magnetic domains. The set-reset coil can be used to reduce the impact of the offset, the hysteresis and other non-linearity effects to the measurement. This is done by measuring the sensor twice, once after a positive pulse and once after a negative one have been applied to the set-reset coil, and by taking their difference as the final outcome [9], [12], [28]–[39]. The offset coil is commonly used to reduce the sensitivity variation and the static nonlinearity of the sensor. This is typically done by operating the sensor in a high-gain closed-loop, where the internal magnetic field generated by the offset coil via feedback current almost cancels the external one [31]–[33]. The closed-loop may be analog or it may include digitization of the signals.

Although the set-reset and offset coils packaged together with the sensing element can be used to achieve superior performance, one should be aware of the electrical and magnetic parasitic coupling between them and between them and the sensing element [27]. The parasitic coupling may impact the measurements or even the stability of the closed-loop, if used. Also, it should be noted that although AMR sensing elements may have an intrinsic bandwidth of up to several MHz [12], [25], [26], [29], fast periodic polarization (set/reset) of the sensing element (with caution not to overheat it), combined with closed loop operation may result in significant reduction of the sensor's effective bandwidth.

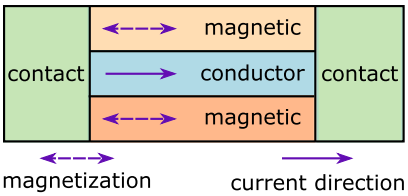

Fig. 3. Typical GMR sensor element structure [12].

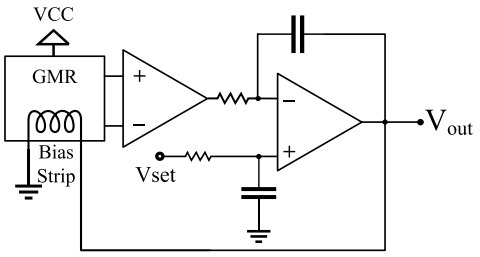

Fig. 4. Example of GMR sensing element in a feedback loop including biasing [49].

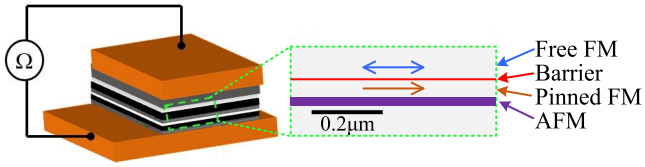

Fig. 5. Structure of a typical TMR sensing element [55].

Modern AMR sensor architectures use periodic alternating (set/reset) polarization in combination with closed loop operation to improve linearity and reduce noise [27], [31], [40]–[42]. Also, biasing of the sensing element is usually done with a constant voltage or current [9], [10], [12], [29], [31], [32]; using AC biasing instead [43], [44] has been proposed to further suppress the sensing element's $1/f$ noise.

B. Giant Magneto-Resistance Sensors (GMR)

The giant magnetoresistance effect refers to the large change of the electrical resistance of a multilayer medium, composed of alternating ferromagnetic and non-magnetic conductive layers, due to an external magnetic field. It was discovered in 1988, by two independent groups; the group of Albert Fert observed the giant magnetoresistance effect on a Fe/Cr(001) multilayer medium while the group of Peter Grünberg worked on a Fe/Cr/Fe(001) three-layer medium [8]–[12], [15].

The operating principle of the GMR sensor is based on the quantum theory of spin-spin interaction between two magnetic layers, the free and the pinned one. As with AMR, GMR sensors also belong to the category of magneto-transport effect sensors [12], [15], [26], [45]–[47]. The simplest GMR sensor consists of two layers of a ferromagnetic material (e.g. Fe-Co-Ni alloy, or a Ni-Fe permalloy) separated by a layer of a conductive material (e.g. Cu or Al) as shown in Figure 3. However, more layers of magnetic and conductive materials are commonly used and new GMR materials such as Co-Fe/Cu are considered to enhance magnetoresistivity [48].

The GMR sensing element is typically used in a Wheatstone bridge configuration. Proper bridge biasing and signal conditioning electronics are essential for quality measurements. As with the AMR sensor, feedback can be used to stabilize the sensitivity (with respect to temperature and other parameters) and suppress the static nonlinearity of GMR sensor, e.g. Figure 4. Also, biasing the GMR sensor bridge with AC current may significantly reduce hysteresis, nonlinearity, offset and noise effects [12], [43], [45]–[47].

C. Tunneling Magneto-Resistance Sensors (TMR)

The Tunneling Magneto-Resistance effect was discovered in 1975 by Michel Jullière in Fe/Ge-O/Co junctions at cryogenic temperatures of 4.2 K [50]. The development of TMR sensors essentially began after 2000 when crystalline magnesium oxide MgO and aluminium oxide (alumina) Al_2O_3 began to be used as the tunnel barrier. From that time on a multitude of new innovations have allowed TMR sensors to achieve more than 600% magnetoresistance ratio [8], [10], [11], [15], [51]–[54].

A typical TMR sensor has three main layers, from bottom to top: a pinned ferromagnetic layer, a tunnel barrier layer, and a free ferromagnetic layer; forming a Magnetic Tunnel Junction (MJT) element. The pinned ferromagnetic layer, at the bottom, is a combination layer formed of an anti-ferromagnetic pinning layer and a ferromagnetic layer. The top ferromagnetic layer is called "free" as its magnetic domains, and therefore its magnetization direction can easily rotate in weak magnetic fields with minimal hysteresis. In contrast, the pinned layer's magnetization direction is relatively fixed in the presence of modest magnetic fields, but can be disturbed in a strong field.

A typical TMR sensor is illustrated in Figure 5. The arrows show the magnetization direction of both the pinned layer and the free layer. The typical thickness of both layers is between 0.1 nm to 100 nm [8], [11], [51]–[54]. Contrary to the GMR, the TMR sensing element is sandwiched between two conductive layers connecting it to the electronic circuit. The structure is usually placed on a substrate, often made of silicon or other materials such as quartz, heat-resistant glass, GaAs and AlTiC [8], [11], [51]–[54].

The TMR sensing element has a resistance in the order of 1 kΩ and can also be used in a Wheatstone bridge configuration with four TMR sensing elements. The noise level of TMR sensors is similar to that of AMR ones [12]. TMR sensor packages may include a coil (often called a set-coil) to polarize the pinned layer as in AMR sensors. A common electronics architecture for operating a Wheatstone bridge TMR sensor with a set-coil is illustrated in Figure 6.

Current research on TMR sensors focuses on the development of new materials for the tunnel barrier layer and the reduction of sensor noise [56]–[58].

D. Hall Effect Sensors

The Hall effect was discovered by Edwin Hall in 1879. It is the generation of a voltage potential on a conductive medium when placed in a magnetic field and an electric current is applied to it. The generated voltage appears in a perpendicular direction to the current and the magnetic field, as shown

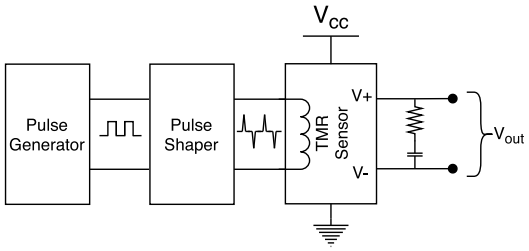

Fig. 6. Typical Architecture of a TMR sensor with a coil [55].

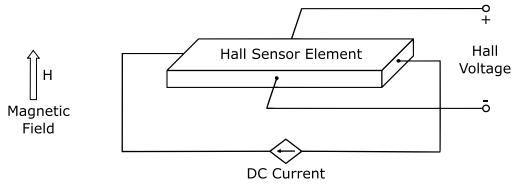

Fig. 7. Hall magnetometer operation principle.

in Fig. 7 [9]–[12]. More precisely, the Hall effect stems from the Lorentz force (or electromagnetic force):

$$\vec{F} = q \cdot \vec{E} + q \cdot \vec{v} \times \vec{B} \tag{1}$$

i.e., a charged particle (electrons in metal conductors, electrons and holes in a semiconductor) moving in a magnetic field, is subject to a force in a direction perpendicular to its motion.

The first generation of Hall effect magnetometers used a thin metal strip excited by a current. Newer generations of Hall effect sensors are constructed using semiconducting materials instead of thin metals. In semiconductors both electrons and holes contribute to the effect. Even though the mobility of electrons in a semiconductor is lower than that in a metal, and holes have even less mobility, the Hall effect is stronger. Lower mobility implies that the charge carriers in a semiconductor sensing element remain in it for longer time resulting in a larger trajectory deviation due to (1) and thus higher sensing gain [9]–[12]. Due to their simple structure and compatibility with standard integration technology, Hall effect sensors can be manufactured massively with very low cost, as semiconductor devices without any extra ferromagnetic material [62].

The greatest advantage of Hall effect sensors when compared to other simple and low-cost solutions (e.g. inductive sensors), is their ability to detect static magnetic fields [18]–[20]. However, there are some aspects that should be taken into account in the sensor's design: 1) The first term of equation (1) impacts the sensor's performance, and special precautions must be taken in the sensor's layout to avoid external electric field interfere with the sensing element. 2) Semiconductors not only have a higher white noise level than conductors due to their higher resistance, but also have additional noise sources such as flicker ($1/f$), shot noise and possibly others. 3) Imbalanced resistive paths in the semiconductor material can lead to offset. 4) Mechanical stress mainly caused by different thermal expansion coefficients of the sensor construction materials can lead to offset stability errors.

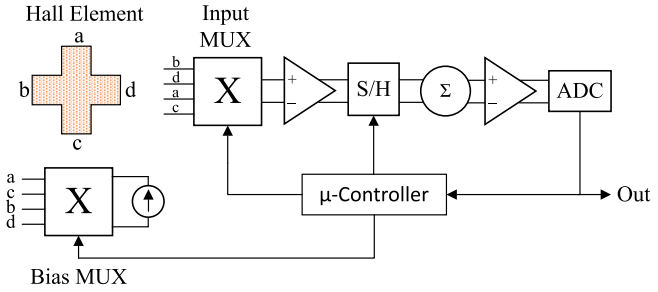

Fig. 8. Hall magnetometer with chopping measurement technique [59]–[61].

To address some of these issues, researchers found out that using chopping techniques and alternating bias current reduces the offset and minimizes the effect of the $1/f$ and shot noise sources improving the Hall sensor's sensitivity. This technique of measuring a Hall sensor is illustrated in Figure 8 and is used in commercial state-of-the-art sensors [59]–[61].

E. Giant MagnetoImpedance Sensors (GMI)

Giant magnetoimpedance is the large change of electrical impedance in certain materials caused by an external magnetic field. The GMI effect was first reported in 1935 by the research team of E. P. Harrison. In the following decades, research on GMI was limited to low frequencies (up to a few hundred Hertz) and only small changes of impedance were reported [8], [12], [63]. In 1994, the research team of F.L.A. Machado measured the GMI effect on thin ribbons and micro-wires of the amorphous soft ferromagnetic material $Co_{70.4}Fe_{4.6}Si_1$ using AC current of frequencies up to $100kHz$ and reporting significant change of the impedance.

Other variations of ferromagnetic materials have been used for GMI sensing elements such as CoFeSi, CoFeCrSiB, CoFeCrSi, FeCuNbMoSiB and other alloys based on Fe or Co. The alloys that present a more profound GMI effect are characterized by negative magnetostriction value [8], [12], [63]–[65]. Since 1994, the advancement of materials science has enabled the development of amorphous wires of significant impedance sensitivity and wide bandwidth (in the MHz range).

The GMI effect is related to the skin effect and is also classified as a magneto-transport effect. When a wire is excited by an AC current, the electric charges tend to move on the surface rather than in the center of the conductor, due to a phenomenon known as skin effect. This results in an increase of the impedance of the wire with increasing frequency. In the case of ferromagnetic wires, the skin effect is stronger in the presence of an external magnetic field (GMI effect). The magnetic domains illustrated in Figure 9 rotate and change shape under the influence of the magnetic field resulting in a change of the wire's impedance.

The simplest GMI sensor is formed of a ribbon made by an amorphous material and excited by an AC current source. As with the AMR sensor, the impedance of the GMI sensing element is an even function of the projected magnetic field on the current flow vector [63]–[65], [67]–[71]. A combination of two or more sensing elements appropriately connected

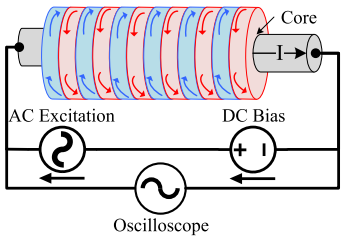

Fig. 9. Typical GMI sensor architecture and operation.

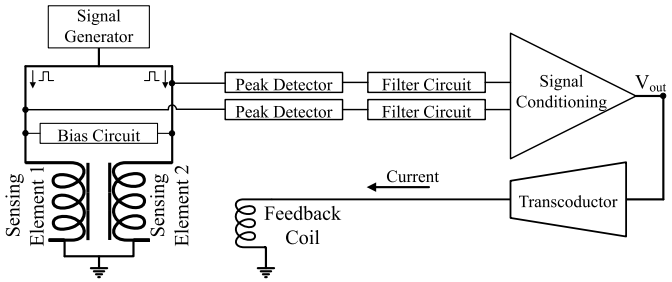

Fig. 10. GMI sensor readout topology [66].

and biased allows for the determination of the field polarity. Figure 10 illustrates a typical GMI sensor with its readout architecture where two GMI sensing elements are used to allow for a differential measurement.

The design of a GMI magnetometer requires special care to the temperature dependency of the GMI effect during operation. Furthermore, in the production process, the connection of the GMI wire to the substrate must be done without heating the wire since heat causes crystallization and therefore loss of the required amorphous properties.

F. Fluxgate Sensors

The first Fluxgate sensor was reported by H.P. Thomas in 1931 while H. Aschenbrenner and G. Goubau were also working on Fluxgate sensors since the late 1920s. During World War II high sensitivity Fluxgate sensors were developed to detect submarines. Since then, Fluxgate sensors have been used in several different fields including geophysical surveys, space exploration and others. The name Fluxgate comes from the gating effect of magnetic flux due to magnetic saturation of the core.

The structure of a basic (parallel) Fluxgate sensor is illustrated in Figure 11. It is composed of two coils wound on a soft magnetic core, the excitation and the sensing one. When a periodic current (AC) passes through the excitation coil, the magnetic material of the core is periodically saturated. The core's saturation leads to a change of its permeability and modulates the magnetic flux associated with the external magnetic field, B_0. The sensor's output is the voltage induced in the sensing coil, the second harmonic of which, is proportional to the external magnetic field.

Fluxgate sensors are divided into two types, the orthogonal and the parallel ones, depending on the orientation of the excitation field (generated by the AC current) with respect to the sensor's sensitivity axis. In the case of orthogonal

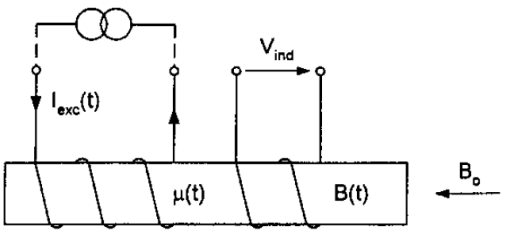

Fig. 11. Basic (parallel) Fluxgate sensor [9].

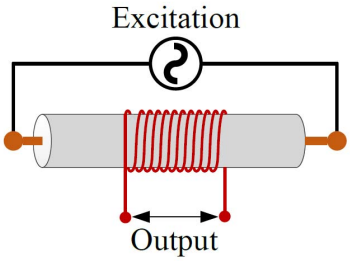

Fig. 12. Typical structure of an orthogonal Fluxgate.

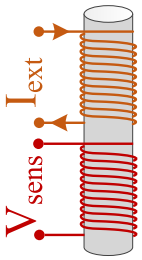

Fig. 13. Typical structure of parallel Fluxgate.

Fluxgates, the excitation field is perpendicular to the sensitivity axis, while in parallel Fluxgates, the excitation field is parallel to the sensitivity axis.

The typical structure of an orthogonal Fluxgate is shown in Figure 12. It is composed of a soft magnetic core excited by an AC current source. Around the core a sensing coil is wound, on which a voltage proportional to the external magnetic field is induced. Due to the better characteristics of the parallel Fluxgates, when compared to orthogonal ones, the latter are not commonly used.

A typical parallel Fluxgate is shown in Figure 13. In this case, two coils are wound around a single, soft magnetic core. By exciting the first coil with an ac source, a voltage proportional to the external magnetic field is induced in the second coil. Parallel Fluxgates are widely used and several different core-coil configurations have been proposed to improve the performance of the basic single-core one. The most popular configurations are shown in Figure 14.

In order to explain the Fluxgate sensor operation, it is helpful to consider a ring core fluxgate as two connected half cores as shown in Figure 15. When an alternating current is applied to the excitation coil, without an external magnetic field, the generated field by each half core is equal in magnitude and opposite in direction, as the two cores go into magnetic saturation concurrently and at the same pace.

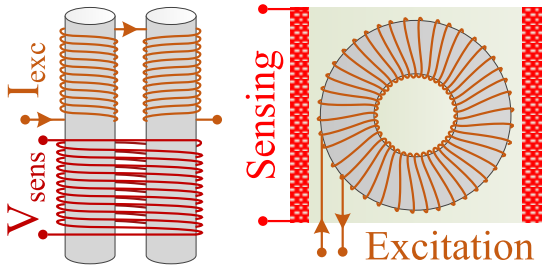

Fig. 14. Indicative parallel Fluxgate core-coil configurations. Dual core (right) and ring core (left) fluxgate sensors.

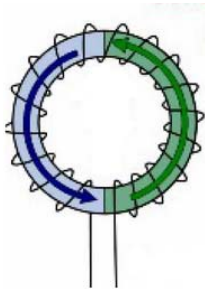

Fig. 15. Ring core Fluxgate split into two half cores.

When an external magnetic field is applied, the half core generating a field in the same direction as the external field saturates faster. However, and because the flux is "gated", the reluctance of the whole magnetic circuit increases and thus the effective permeability of the second half core rapidly decreases. This can be seen in Figure 16 as a shift of the B-H loop. [9]–[12], [72]–[75].

Fluxgate sensors are rarely used in an open-loop architecture. Instead a closed-loop architecture is preferred, where a current proportional to the measurement is fed back to the sense coil (or a third coil coupled to the core) generating a magnetic field component opposite to the external one [76]–[79]. Closed-loop operation improves the linearity and the input measurement range of the sensor [80], [81].

A typical Fluxgate sensor system using a ring-core parallel Fluxgate is illustrated in Figure 17. A periodic signal drives the excitation coil. Then, a synchronous detector is used to capture the amplitude of the second harmonic of the induced voltage in the sensing coil. The low-pass-filtered amplitude-waveform of the second harmonic, from the synchronous detector, is the sensor's output signal. Finally, the loop is closed by feeding the output back to the sensing coil.

The frequency of the excitation signal is typically limited to 10-100 kHz due to the coil's parasitics and the high core magnetization that creates eddy currents. In this frequency range, the soft magnetic material of the core has maximum permeability and the eddy currents in the core are low. The typical bandwidth of commercial fluxgates is usually about 1 kHz while the maximum reported in literature is about 10 kHz [9]–[12].

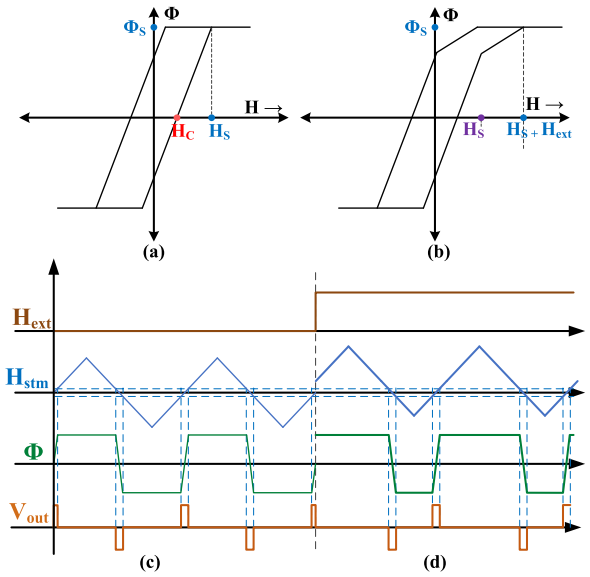

Fig. 16. Core's magnetic flux density without (a) and with (b) external magnetic field along with the corresponding waveforms (c,d) [9].

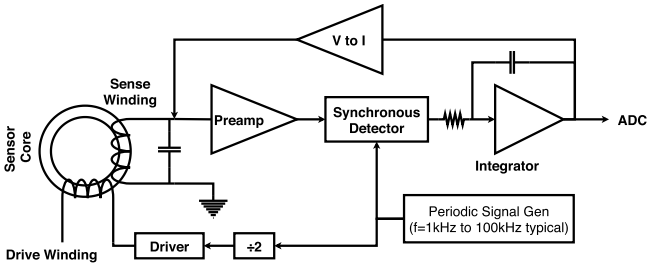

Fig. 17. Ring core fluxgate sensor and typical front-end circuit architecture based on the second harmonic [82].

G. Search Coils

The Search Coils or Induction sensors are some of the most sensitive magnetometers and are usually quite simple to build. They are based on the Induction Law measuring the varying magnetic flux. They date back to 1831, when the first experiments with electric and magnetic fields took place by Michael Faraday [1]–[8], [12], [83]–[85].

They have a very low noise floor and are linear when no ferromagnetic material is used, but they cannot measure DC and very low frequency magnetic fields. They can be classified in four major categories according to whether they are passive or active and whether they have a ferromagnetic core or not [5]–[12].

Active Search Coils are typically used for metal detection or for proximity detection. In this case two coils are used, one for excitation and one for reception. When a metal comes near the coils it changes the coupling coefficient and therefore the voltage of the reception coil. A ferromagnetic core is used to increase sensitivity (and measure weaker magnetic fields) and/or extend the operating range to lower frequencies. Soft magnetic materials of high permeability are typically preferred.

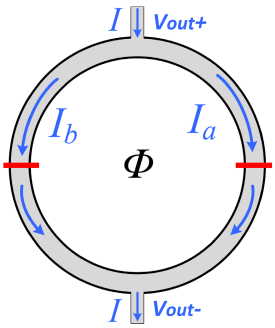

Fig. 18. Typical structure of a SQUID magnetometer.

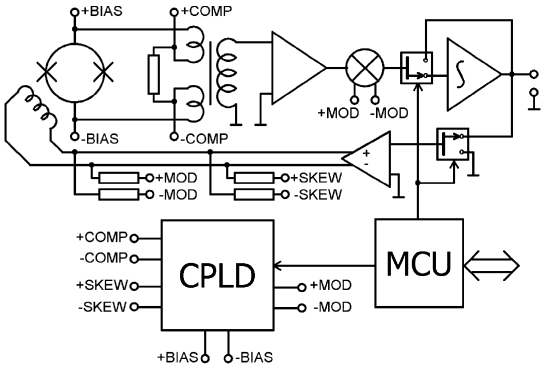

Fig. 19. SQUID magnetometer measurement topology [96].

H. SQUID Sensors

A Superconducting Quantum Interference Device (SQUID) is an extremely sensitive magnetic sensor based on superconducting loops containing Josephson junctions. The structure of a typical SQUID sensor is shown in Figure 18. The development of SQUID sensors followed the theoretical work on superconductivity and electron pair tunneling in the late 1950s and early 1960s [9], [10], [12].

The theory of operation of SQUIDs is complex and a deep knowledge of quantum theory is required to grasp it. Briefly, a SQUID sensor is composed of a super conductive loop that contains two Josephson junctions.

In order for a SQUID sensor to work properly, it needs to be cooled down to cryogenic temperatures where the vibration of the crystal lattice (phonon vibrations) is reduced and superconductivity kicks in. If the SQUID sensor is made of a Type I Superconductor it requires extremely low temperatures (below 4 K) thus liquid helium must be used with a great increase in operating cost. A compromise can be made by using Type II Superconductors, in which case liquid nitrogen (at 77 K) can be used with an increase in measurement noise due to higher temperature.

When cooled to a sufficiently low temperature, the loop becomes superconductive, expelling any magnetic flux from its material and trapping it in the center of the loop. The value of this flux can only be a multiple of the flux quantum $\phi_0 = h/2e$, where h is Planck's constant, $h = 6.624 \cdot 10^{-34} Js$, and $e = 1.602 \cdot 10^{-19} C$ is the charge of the electron, [25], [26].

According to Cooper pair theory [25], [26], [86]–[88], two electrons can form a pair through electron-phonon interaction, causing them to behave as an entity. If there is no external magnetic field the current passing through one branch (I_a) will be the same as the current through the other (I_b).

When an external magnetic field is applied, the superconductive loop expels the magnetic field from the center of the loop in discrete levels $n \cdot \phi_0$, as mentioned above. In this case, a pair of electrons will appear and begin cycling the loop in order to cancel out the external magnetic field. Now (I_a) will not equal (I_b) and a voltage will be generated across the SQUID terminals as illustrated in Figure 18. This is due to the Josephson effect, where the current can pass through the non-superconductive junction barrier by quantum tunneling, thus creating a voltage difference without limiting the current [9], [10], [12], [26].

The SQUID is one of the most sensitive magnetometers, able to measure extremely low magnetic fields. It also has an upper detection limit at which point the superconductor reverts to normal conductivity [9], [12], [26], [89]. A diagram of a typical SQUID magnetometer is shown in Figure 19. The output voltage of a SQUID cannot be easily correlated with the applied magnetic field due to quantization, hysteresis and the initial conditions of the SQUID. A closed loop architecture is preferred and the output voltage is typically fed to a PID controller generating a feedback current through a coil coupled to the SQUID, which ideally annihilates the magnetic field in the SQUID [90], [91].

Research on SQUID sensors is focused on further development of superconductor materials and the complete modeling of the sensor in order to allow for magnetic field measurements without the need of external magnetic shielding [92]–[95].

I. Other Types of Magnetic Field Sensors

There are many other types of magnetic field sensors not included in this review, because they are rarely used or they are designed for very specific applications. These types of sensors include the magneto-diode, magneto-transistor, magnetostriction-piezoelectric and crystal magnetometers as well as sensors based on the following physical phenomena: MEMS Lorentz Force, nonlinear magneto-optical rotation, Nitrogen-Vacancy Centers in Diamond, spin exchange relaxation free (SERF), helium magnetic resonance, magneto-elastic field, nuclear precession [8], [9], [12], [26], [86], [87].

J. Magnetic Field Sensors Comparison

Due to the great variation in properties and cost of the different magnetic field sensors, the selection of an appropriate sensor is highly application dependent. One can start with considering the magnetic field range different sensor types can measure, as shown in Figure 20. Linearity, effective frequency bandwidth, scalability, cost, physical dimensions, robustness and tolerance to environmental conditions are some other aspects one should also consider. Table I presents some of the main characteristics of various commercially available sensors of different types.

III. Calibration Techniques

The magnetic field sensor technologies presented in Section II are used in a wide range of applications, from

TABLE I
COMPARISON OF BASIC PERFORMANCE CHARACTERISTICS OF BOTH COMMERCIAL AND EXPERIMENTAL MAGNETIC FIELD SENSORS

	AMR[1]	GMR	TMR	GMI
Sensors	[97]	[98]	[99]	[100]
Magnetic Field Range	200 μT	0.15 mT - 1.05 mT	$\leqslant$ 0.8 mT	$\leqslant$ 1.2 mT
Bandwidth @-3dB	DC - 5 MHz	500 kHz	—	$\leqslant$ 500 Hz *
Resolution	—	—	—	12 bit
Noise level (Trms/$\sqrt{Hz}$)	$\leqslant$190p @ 1 Hz	—	150p @ 1 Hz	—
Offset Error	$\leqslant$59 μT	$\leqslant$ 95 μT	$\leqslant$ 15 μT	$\leqslant$ 170 nT
Hysteresis	$\leqslant$300 nT	—	2μT	—
Axes Alignment Error	—	—	—	—
Scaling Error	—	$\leqslant$ 14%	—	—
Linearity Error	$\leqslant$2%	—	$\leqslant$ 0.5%	$\leqslant$ 0.5%
Temperature coefficient of scale factor	$\leqslant$3000 ppm/°C	—	$\leqslant$ -300 ppm/° C	1400 ppm /°C *
Power Consumption	$\approx$ 29 mW *	$\approx$ 110 mW *	$\approx$ 70 μ W *	—

	HALL	Fluxgate	Search Coil	SQUID
Sensors	[101]	[102]	[103]	[104]
Magnetic Field Range	10mT	75μT		2.5 μT
Bandwidth @-3dB	DC - 53 kHz *	DC - 1.5 kHz	250 μHz - 10 kHz	DC - 10 kHz
Resolution	—	—	—	—
Noise level (Trms/$\sqrt{Hz}$)	—	$\leqslant$ 4p @ 1 Hz	$\leqslant$ 0.3p @ 1 Hz	55f @ 1 Hz
Offset Error	$\leqslant$ 320 μT	$\leqslant$ 40 nT	—	—
Hysteresis	—	—	—	—
Axes Alignment Error	—	$\leqslant$1°	—	—
Scaling Error	$\leqslant$ 2%	$\leqslant$ 0.75%	—	—
Linearity Error	$\leqslant$ 0.8%	$\leqslant$ 0.015%	—	—
Temperature coefficient of scale factor	$\leqslant$ 200 ppm/° C	$\leqslant$ 70 ppm/°C	—	—
Power Consumption	$\approx$ 120 mW *	$\approx$ 650 mW *	$<$ 225 mW	$\leqslant$ 225 mW (+7kW)*

The authors tried to collect the specifications of each sensor. Some values (marked with "*") have been calculated based on the specifications provided by the manufacturer and may be indicative and not exact.

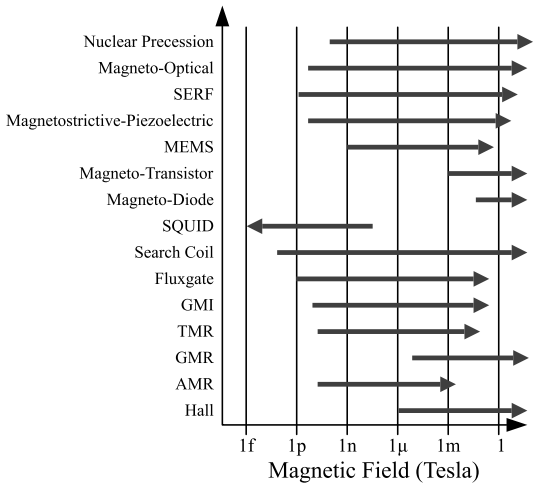

Fig. 20. Magnetic field measurement range of different sensors at typical operating conditions.

low-cost portable systems (smartphones, activity trackers etc.) to high-end industrial, marine and military applications. Although different types of magnetic field sensors vary significantly in measurement accuracy and cost, they all require a calibration procedure to provide accurate measurements.

The purpose of the magnetic field sensors' calibration is twofold. First, as in every measurement unit, calibration ensures that each measurement corresponds to the actual value of the measured quantity and it is not affected by other static (manufacturing imperfections etc.) or dynamic (temperature, humidity, etc.) parameters. In addition, when embedded in a larger system, magnetic field sensor's measurements are also distorted by external magnetic disturbances, typically caused by the system's enclosure and surrounding electronic components. This distortion is in several cases the main contributor to the overall measurement error and thus it must also be canceled during calibration.

A. Magnetic Field Sensor's Errors and Measurement Model

The first step of every calibration technique is to derive a mathematical model describing the most important time-invariant sensor's errors including the external magnetic disturbances. The error of a 3-axis magnetic sensor is most commonly expressed as a mixture of the following error components:

- Offset: A constant additive bias at the sensor's output exhibited by all types of magnetic sensors. It is typically the main contributor of the total measurement error. Offset is modeled by a 3×1 vector (h_m).
- Scale factor error: It is the deviation of the input-output gain from unity. A 3×3 diagonal matrix (T_{sf}) is typically used to model its effect on the measurement.
- Cross-coupling error: It is caused by the imperfect alignment of the sensor's axes during its manufacturing. It is modeled by a 3×3 matrix (T_{cc}).

[1]Please note that the HMC 1001 Sensor is an AMR sensing element, not a complete sensor system. Integration into a complete sensor system (with the required instrumentation electronics) is expected to improve its performance.

- Random noise: It is the non-deterministic error caused by both the mechanical and the electronic structures of the sensor. It is modeled by a 3×1 random vector (n).

When the sensor is embedded in a system, the surrounding magnetic and ferromagnetic materials, fixed on the sensor's platform, distort the local magnetic field causing an additional measurement error. This distortion is divided into two types: soft-iron distortion and hard-iron distortion.

Soft-iron distortion is caused by ferromagnetic materials attached on the sensor's platform. While such materials do not generate a magnetic field themselves, they alter the existing magnetic field causing an error to the sensor's measurement. The effect of the soft-iron distortion is modeled by a 3×3 matrix (T_{si}).

Hard-iron distortion is caused by the magnetic materials attached on the sensor's platform. They generate a constant magnetic field resulting in a constant offset. Similarly to the sensor's inherent offset, hard-iron distortion is modeled by a 3×1 vector (h_{hi}).

Considering the aforementioned error terms, the 3×1 measurement vector y is related to the 3×1 magnetic field vector m as follows [105]–[112]

$$y = T_{sf} T_{cc} \left(T_{si} m + h_{hi}\right) + h_m + n \tag{2}$$

For calibration purposes it is not required to calculate the exact contribution of each error term and thus the compact form of (3) is most commonly used

$$y = Tm + h + n \tag{3}$$

where $T \triangleq T_{sf} T_{cc} T_{si}$ and $h \triangleq T_{sf} T_{cc} h_{si} + h_m$. Note that the measurement model of (3) is also valid in the case of a 2-axis or a single-axis magnetic sensor with proper sizing of the parameters T and h.

B. Calibration Using Special Equipment

Given the measurement model of (3), the calibration procedure aims to derive parameters T and h. This can be done using a set of measurements, y_k corresponding to known magnetic field vectors $m_k, k = 1, 2, \ldots, K$. Such measurements are typically performed in a magnetically shielded chamber where 3D coil structures are used to generate m_k.

Magnetic shielding (or magnetic cleanliness) is achieved using a Gauss chamber which is designed to block the external magnetic field. Several different technologies of Gauss chambers are available. They are divided in two main categories; passive and active ones. Passive Gauss chambers are constructed using several layers of suitable metals to attenuate the external magnetic field. Active ones use a high-accuracy magnetic sensor and a 3D coil structure (typically a Helmholtz coil setup) in a closed-loop configuration to cancel out the external magnetic field.

To generate a known magnetic field vector, a 3D Helmholtz coil setup is most commonly used. A 3D Helmholtz coil is comprised of three pairs of identical circular coils placed symmetrically along a common axis as shown in Figure 21. When the coils are excited with a DC current, a constant, nearly uniform magnetic field is generated in a small region close to the center of the setup. The region and the degree of uniformity are mainly dictated by the geometrical characteristics of the coils. An improvement to the Helmholtz coils are the Maxwell coils, the structure of which is also shown in Figure 21. Maxwell coils provide a more uniform magnetic field than the Helmholtz ones but they are not as common due to their higher complexity and cost.

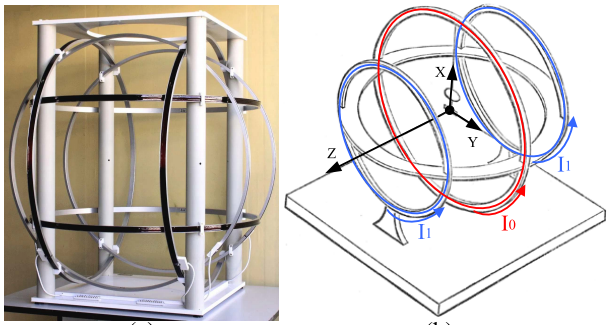

Fig. 21. Typical structure of a Helmholtz Coil (model BH1300-3-A of ASC Scientific) (left) - Maxwell Coil (right).

C. Equipment-Free Calibration

The advancement of MEMS technology over the past decades significantly broadened the application span of the magnetic sensors. Along with MEMS inertial sensors (accelerometers and gyroscopes) they are nowadays used in a wide range of low-cost, commercial devices. In such cases, factory calibration, or post-production calibration using special equipment are prohibited as they significantly raise the sensor's cost. To this end, many magnetic sensors calibration methods, not using any special piece of equipment, have been reported in the literature.

The main idea behind most of these methods is to exploit the earth's magnetic field as a reference. As it varies with location and time, its value (direction and magnitude) is only approximately known from magnetic models such as World Magnetic Model (WMM) and International Geomagnetic Reference Field (IGRF). However, should the calibration procedure take a very short time (compared to the rate of change of the earth's magnetic field) and performed away from any magnetic disturbances, it is reasonable to assume that the magnitude of the local magnetic field is constant during the calibration procedure.

The locally constant magnitude of the magnetic field, along with the measurement model (3) and a set of several measurements $y_k, k = 1, 2, \ldots, K$ in different orientations are combined to formulate the following optimization problem for deriving the calibration parameters T and h.

$$\text{minimize} \sum_{k=1}^{N} \|y_k - Tm_k - h\|^2 \tag{4}$$

$$\text{subject to } \|m_k\| = 1, \quad k = 1, 2, \ldots, N \tag{5}$$

Note that in (4) both the calibration parameters T and h and the magnetic field vectors, m_k are unknown. What is known is the constant magnitude of the vectors, m_k, which

can be considered normalized. Several works propose different solutions to (4) or a variation of it. In [106], [107], [110], [112]–[114], a solution to (4) is derived by using the gradient descent or the Newton–Raphson method where the initial conditions should be properly selected to ensure (fast) convergence. Iterative algorithms based on the least-squares method are proposed in [105], [115]–[117] achieving increased computational efficiency, especially in the case of big datasets.

D. Magnetic - Inertial Sensors Axes Alignment

Magnetic and inertial sensors are commonly combined in several applications. In such cases, other than the individual calibration of the magnetic sensor, an extra step of aligning its sensitivity axes with those of the inertial sensors, is required.

Axes alignment is a straight forward procedure when expensive calibration equipment is used (rate-table, Helmholtz coils setup, Gauss chamber etc.). In this case the calibration equipment provides a well-defined coordinate system. The axes alignment between the sensors is achieved by aligning all the sensors to the coordinate system of the calibration equipment.

In contrast, when low-cost sensors are concerned, both the calibration of the magnetic and inertial sensors and the alignment of their axes are commonly done without using any special piece of equipment. This can be done by exploiting the magnetic inclination phenomenon (or the presence of a constant and locally uniform magnetic field in general) and several accelerometer and magnetometer measurements. Most authors either fuse the calibration of magnetic and inertial sensors into a single algorithm, incorporating the axes alignment step [106], [109], [118]–[121], or individually calibrate inertial and magnetic sensors and then align their axes as a discrete step [105], [111], [122], [123].

IV. Magnetic Field Sensors Applications

Due to their versatility and usefulness, magnetic field sensors have a multitude of applications. As each type of magnetic field sensor has different specifications (resolution, noise, accuracy,etc) their applications vary accordingly. In this section some of the applications of each sensor type are presented.

A. AMR - GMR - TMR

Due to their operation, AMR, GMR and TMR sensors have relatively similar applications. AMR and GMR sensors can be built as a chip, allowing for low cost applications. Thanks to their small size, single layer construction and very low noise, AMR sensors are widely used in the industry and mainly in the space and automotive ones. Due to the rise of nano and pico sats (artificial satellites with very small size and low wet mass when compared to traditional ones), AMR sensors are starting to replace fluxgate sensors as the magnetic field sensor of choice for satellites [124]. In the automotive industry, AMR sensors are becoming the de facto choice for a magnetic field sensor, especially due to work being done on their dependability and fault-tolerance [125]. Finally, the rise of smart grids in the last few years has created a new market for AMR sensors in the form of current meters for power meters [126].

GMR sensors can provide higher signals at lower field levels while being relatively immune to temperature swings [127]. Their most prominent uses are for position detection and as isolators in electronic circuits. In the first case, GMR sensors allow for the detection of the relative position of wheels (and thus determine speed and acceleration as well), pneumatics and even cars [128], [129]. In the second case, GMR sensors allow for the inclusion of isolated sections in integrated circuits, often with switching speeds that exceed those of optoisolators [130].

TMR sensors have started to replace GMR sensors in applications such as hard disk drive heads, angular position sensors, magnetic switches and others. However high-quality TMR sensors intended for magnetic field measurements are still expensive and thus AMR sensors are usually preferred.

B. Hall

The main characteristics of Hall effect sensors are their very low cost and ease of manufacturing. They have been widely employed in the industry as position sensors and gear tooth counters [131]. One of their most common uses is for the closed loop feedback of brushless motors [132]. They have also been used in power meters for the isolated measurement of current [101], [133].

C. GMI

GMI sensors exhibit extremely high sensitivity, on par with flux gate sensors, coupled with a very small size [66], [100]. GMI sensors also allow for very high frequency measurements in the range of 10MHz [134]. However due to difficulty integrating the sensing wire, GMI sensors have limited use. They are mainly used for research purposes. One commercial use is in continuous tyre pressure monitoring systems that can operate without an integrated battery [63].

D. Fluxgate

Even though fluxgate sensors are a relatively older and simpler design, they are still widely used. Their miniaturization potential along with their low power consumption and ruggedness, allow for portable applications [102], [135], [136]. Fluxgate sensors can be used for motion tracking, digital navigation in mobile devices and non-destructive testing [137]–[139]. They are also used for archaeological prospecting and unexploded ordinance (UXO) detection [140].

E. Search Coil

Active search coils are usually used for metal detection, position detection and for Non-Destructive Testing (NDT). They are the sensing elements of Barkhausen Noise measurement systems and they can be used to identify the B-H loop of a bulk material. Search Coils of this type can also be used for position measurements between the sensor and a metallic plate. Search Coils with a ferromagnetic core are more sensitive than those with an air core due to the high permeability of the core. However, they suffer from 1/f noise due to the Barkhausen effect of the core when the latter is

magnetized and demagnetized. In addition, due to their core structure they exhibit small amounts of hysteresis. The Search Coil sensor with an air core is usually used for measuring the AC magnetic field produced by Electromagnetic Emission (EM waves) not only in a laboratory setting but also in the field. Moreover, they are also used for geophysical purposes such as Magnetotellurics (MT) in underground and surface stations. They are the main method (combined with acoustic waves) for determining the place of the drilling bit in the petroleum industry [10], [11], [85], [141]–[143]. In the same industry they are also used to map the wells and land.

F. SQUID

Even though the cost of SQUID sensors is high (both for their operation as they require liquid helium as well as for their manufacture) they are extensively used in areas where extreme sensitivity and measurement accuracy are of paramount importance. Due to the SQUID sensor's ability to detect minimal changes in magnetic field it is used as a biosensor and specifically for magnetoencephalography [144], [145] and also for the detection of magnetic nanoparticles used for homogeneous immunoassay [146]. The SQUID sensor has also been used for the exploration of mineral resources [147]. It has also been used in theoretical physics experiments [148].

REFERENCES

[1] W. Gilbert, *De Magnete*. New York, NY, USA: Dover, 1991.
[2] D. J. Jackson, *Classical Electrodynamics*, 3rd ed. San Francisco, CA, USA: Wiley, 1999.
[3] S. Blundell, *Magnetism: A Very Short Introduction*. London, U.K.: Oxford Univ. Press, 2012.
[4] A. Garg, *Classical Electromagnetism*, I. A. Nutshell, Ed. Woodstock, U.K.: Princeton Univ. Press, 2012.
[5] M. Getzlaff, *Fundamentals Magnetism*, 1st ed. Berlin, Germany: Springer, 2008.
[6] S. Chikazumi, *Physics of Ferromagnetism*. New York, NY, USA: Oxford Univ. Press, 1997.
[7] C. Kittel, *Introduction to Solid State Physics*, 8th ed. Hoboken, NJ, USA: Wiley, 2005.
[8] S. Tumannski, *Handbook of Magnetic Measurements*. Boca Raton, FL, USA: CRC Press, 2011.
[9] P. Ripka, *Magnetic Sensors Magnetometers*. Boston, MA, USA: Artech House, 2001.
[10] P. Ripka and A. Tipek, *Modern Sensors Handbook*, P. Ripka and A. Tipek, Eds. London, U.K.: ISTE, Jan. 2007.
[11] J. Fraden, *Handbook Modern Sensors*, 4th ed. New York, NY, USA: Springer, 2010.
[12] A. Grosz, M. J. Haji-Sheikh, and S. C. Mukhopadhyay, *High Sensitivity Magnetometers*, vol. 19, 1st ed. Palmerston North, New Zealand: Springer, 2017.
[13] B. Aktas, L. Tagirov, and F. Mikailov, *Magnetic Nanostructures*, 1st ed. Berlin, Germany: Springer, 2007.
[14] B. D. Cullity and C. D. Graham, *Introduction to Magnetic Materials*, 2nd ed. Hoboken, NJ, USA: Wiley, 2009.
[15] S. Kasap, *Principles of Electronic Materials and Devices*, 4th ed. New York, NY, USA: McGraw-Hill, 2018.
[16] J. C. Mallinson, *The Foundations of Magnetic Recording*. Amsterdam, The Netherlands: Elsevier, 1993.
[17] A. Ktena, "Physics and modeling of magnetic non destructive testing techniques," *Key Eng. Mater.*, vol. 495, pp. 265–268, Nov. 2011.
[18] FrSky. *FrSky MC12P Hall Sensor Gimbal*. [Online]. Available: https://www.horusrc.com/en/frsky-mc12p-hall-sensor-gimbal.html
[19] Magcam. *Magnetic Camera*. [Online]. Available: https://www.magcam.com/product/Minicube3D
[20] Honeywell Ind. *Non-Contact Hall-Effect Rotary Position Sensors*. [Online]. Available: https://sensing.honeywell.com/sensors/non-contact-hall-effect-rotary-position-sensors
[21] Sensitec GmbH. *Specific Design Features*. [Online]. Available: https://aerospace.honeywell.com/en/
[22] Z. Zhenhong, O. Syuji, A. Osamu, and K. Hideto, "Development of the highly precise magnetic current sensor module of ± 300 A utilizing AMR element with bias-magnet," *IEEE Trans. Magn.*, vol. 51, no. 1, pp. 1–5, Jan. 2015.
[23] Z. Zhang, M. Tao, and H. Yuan, "A parking occupancy detection algorithm based on AMR sensor," *IEEE Sensors J.*, vol. 15, no. 2, pp. 1261–1269, Feb. 2015.
[24] M. M. Prudenziati, *Thick Film Sensors*. Amsterdam, The Netherlands: Elsevier, 1994.
[25] H. J. García and I. L. Markov, "Spinto: High-performance energy minimization in spin glasses," in *Proc. Design, Autom. Test Eur. (DATE)*, Mar. 2010, pp. 160–165.
[26] S. Kusminskiy, *Quantum Magnetism, Spin Waves, and Optical Cavities*. Cham, Switzerland: Springer, 2019.
[27] N. G. Hadjigeorgiou and P. P. Sotiriadis, "Parasitic capacitances, inductive coupling, and high-frequency behavior of AMR sensors," *IEEE Sensors J.*, vol. 20, no. 5, pp. 2339–2347, Mar. 2020.
[28] H. Hauser, J. Hochreiter, G. Stangl, R. Chabicovsky, M. Janiba, and K. Riedling, "Anisotropic magnetoresistance effect field sensors," *J. Magn. Magn. Mater.*, vols. 215–216, pp. 788–791, Jun. 2000.
[29] Honeywell Ind. *1 and 2 Axis Magnetic Sensors HMC100X*. [Online]. Available: https://aerospace.honeywell.com/en/
[30] Honeywell. (2005). *Application Notes for AMR*. [Online]. Available: https://aerospace.honeywell.com/
[31] N. Hadjigeorgiou, E. Hristoforou, and P. P. Sotiriadis, "Closed-loop current-feedback, signal-chopped, low noise AMR sensor with high linearity," in *Proc. 6th Int. Conf. Modern Circuits Syst. Technol. (MOCAST)*, May 2017, pp. 2020–2023.
[32] I. Georgakopoulos, N. Hadjigeorgiou, and P. P. Sotiriadis, "A CMOS closed loop AMR sensor architecture," in *Proc. Panhellenic Conf. Electron. Telecommun. (PACET)*, Nov. 2017, pp. 1–4.
[33] D. Novotny, V. Petrucha, and M. Janosek, "A digitally compensated AMR magnetometer," *IEEE Trans. Magn.*, vol. 55, no. 1, pp. 1–5, Jan. 2019.
[34] V. Petrucha, V. Fura, and A. Platil, "Cross-field effect in a triaxial AMR magnetometer with vector and individual compensation of a measured magnetic field," *IEEE Trans. Magn.*, vol. 53, no. 4, Oct. 2017, Art. no. 4000305.
[35] J. Ouyang, S. Chen, Y. Zhang, F. Jin, and X. F. Yang, "Measurement of the anisotropy fields for AMR sensors," in *Proc. IEEE Int. Conf. Electron Devices Solid-State Circuits (EDSSC)*, no. 5, Nov. 2011, pp. 21–22.
[36] T. Halim and K. Leitis, "Digitizing the feedback signal in a magnetic field (AMR) sensor system using delta sigma modulator topology," in *Proc. Int. SoC Design Conf. (ISOCC)*, 2012, pp. 112–115.
[37] P. Ripka, M. Janošek, and M. Butta, "Crossfield sensitivity in AMR sensors," *IEEE Trans. Magn.*, vol. 45, no. 10, pp. 4514–4517, Oct. 2009.
[38] A. Zambrano and H. G. Kerkhoff, "Online digital compensation method for AMR sensors," in *Proc. IFIP/IEEE Int. Conf. Very Large Scale Integr. (VLSI-SoC)*, Sep. 2016, pp. 1–6.
[39] K. Leitis and T. Halim, "Modeling of a 3D magnetic field (AMR) sensor," in *Proc. IEEE Int. Conf. Microw., Commun., Antennas Electron. Syst. (COMCAS)*, Nov. 2011, pp. 1–4.
[40] P. Ripka, J. Vyhnanek, M. Janosek, and J. Vcelak, "AMR proximity sensor with inherent demodulation," *IEEE Sensors*, vol. 14, no. 9, pp. 3119–3123, Sep. 2013.
[41] N. Hadjigeorgiou, K. Papafotis, and P. P. Sotiriadis, "Exploring AMR sensors performance limits using an agile, high-speed set-reset pulse generation circuit," *IEEE Trans. Magn.*, vol. 56, no. 9, pp. 1–10, Sep. 2020.
[42] NASA. *Wide Bandwidth Magnetoresistive Eddy Current Probe*. [Online]. Available: https://technology.nasa.gov/patent/LAR-TOPS-96
[43] P. Ripka, M. Tondra, J. Stokes, and R. Beech, "AC-driven AMR and GMR magnetoresistors," *Sens. Actuators A, Phys.*, vol. 76, nos. 1–3, pp. 225–230, Aug. 1999.
[44] Y. Liu, X. Li, and X. Wang, "Bias voltage correction of HMC1022 AMR sensor," in *Proc. IEEE Int. Conf. Mechatronics Autom.*, Aug. 2011, pp. 1550–1554.
[45] C. Reig, S. Cardoso, and S. C. Mukhopadhyay, *Giant Magnetoresistance (GMR) Sensors* (Smart Sensors, Measurement and Instrumentation), vol. 6. Berlin, Germany: Springer, 2013.
[46] M. Djamal and Ramli, "Development of sensors based on giant magnetoresistance material," *Procedia Eng.*, vol. 32, pp. 60–68, 2012. [Online]. Available: http://www.sciencedirect.com/science/article/pii/S1877705812012684, doi: 10.1016/j.proeng.2012.01.1237.

[47] D. Singh, R. Roy, and M. Senthil Kumar, "Magnetic and magnetotransport study of Si/Ni multilayers correlated with structural and microstructural properties," *J. Magn. Magn. Mater.*, vol. 497, Mar. 2020, Art. no. 166053.

[48] M. Milyaev, L. Naumova, V. Proglyado, T. Krinitsina, N. Bannikova, and V. Ustinov, "High GMR effect and perfect microstructure in CoFe/Cu multilayers," *IEEE Trans. Magn.*, vol. 55, no. 4, pp. 1–4, Apr. 2019.

[49] A. Bernieri, L. Ferrigno, M. Laracca, and A. Tamburrino, "Improving GMR magnetometer sensor uncertainty by implementing an automatic procedure for calibration and adjustment," in *Proc. IEEE Instrum. Meas. Technol. Conf. (IMTC)*, May 2007, pp. 1–6.

[50] M. Julliere, "Tunneling between ferromagnetic films," *Phys. Lett. A*, vol. 54, no. 3, pp. 225–226, Sep. 1975.

[51] S. Ikeda *et al.*, "Tunnel magnetoresistance of 604% at 300 K by suppression of Ta diffusion in CoFeB/MgO/CoFeB pseudo-spin-valves annealed at high temperature," *Appl. Phys. Lett.*, vol. 93, no. 8, pp. 1–4, 2008.

[52] T. Miyazaki and N. Tezuka, "Giant magnetic tunneling effect in Fe/Al2O3/Fe junction," *J. Magn. Magn. Mater.*, vol. 139, no. 3, pp. L231–L234, Jan. 1995.

[53] M. Bowen *et al.*, "Large magnetoresistance in Fe/MgO/FeCo(001) epitaxial tunnel junctions on GaAs(001)," *Appl. Phys. Lett.*, vol. 79, no. 11, pp. 1655–1657, Sep. 2001.

[54] N. Zhang, C. Ye, L. Peng, and Y. Tao, "Eddy current probe with three-phase excitation and integrated array TMR sensors," *IEEE Trans. Ind. Electron.*, early access, Apr. 28, 2020, doi: 10.1109/TIE.2020.2989704.

[55] M. Dimension. (2019). *TMR Sensor*. [Online]. Available: http://www.dowaytech.com

[56] J. Zhou *et al.*, "High tunnel magnetoresistance in Mo/CoFe/MgO magnetic tunnel junction: A first-principles study," *IEEE Trans. Magn.*, vol. 53, no. 11, pp. 1–4, Nov. 2017.

[57] H. Lee, H. Sukegawa, J. Liu, Z. Wen, S. Mitani, and K. Hono, "Tunnel magnetoresistance of ferromagnetic antiperovskite MnGaN/MgO/CoFeB perpendicular magnetic tunnel junctions," *IEEE Trans. Magn.*, vol. 52, no. 7, pp. 1–4, Jul. 2016.

[58] V. Venugopal, G. Wu, S. Stokes, and H. Yin, "Pattern dependence of TMR sensor noise," *IEEE Trans. Magn.*, vol. 51, no. 11, pp. 1–4, Nov. 2015.

[59] A. Bilotti, G. Monreal, and R. Vig, "Monolithic magnetic Hall sensor using dynamic quadrature offset cancellation," *IEEE J. Solid-State Circuits*, vol. 32, no. 6, pp. 829–835, Jun. 1997.

[60] S.-M. Lim and J.-S. Park, "A low noise offset cancellation method for improving sensitivity of CMOS Hall sensor," *J. Electr. Eng. Technol.*, vol. 14, no. 1, pp. 377–383, Jan. 2019.

[61] M. Motz *et al.*, "A miniature digital current sensor with differential Hall probes using enhanced chopping techniques and mechanical stress compensation," in *Proc. IEEE Sensors*, Oct. 2012, pp. 26–29.

[62] Honeywell Ind. (2010). *Hall Effect Sensing and Application*. [Online]. Available: https://sensing.honeywell.com/hallbook.pdf

[63] M.-H. Phan and H.-X. Peng, "Giant magnetoimpedance materials: Fundamentals and applications," *Prog. Mater. Sci.*, vol. 53, no. 2, pp. 323–420, Feb. 2008.

[64] P. Ripka, A. Platil, P. Kaspar, A. Tipek, M. Malatek, and L. Kraus, "Permalloy GMI sensor," *J. Magn. Magn. Mater.*, vols. 254–255, pp. 633–635, Jan. 2003.

[65] H. Hauser, I. Giouroudi, J. Steurer, L. Musiejovsky, and J. Nicolics, "Magnetic hysteresis modeling of giant magnetoimpedance thin films," *Sensor Lett.*, vol. 5, no. 1, pp. 133–137, Mar. 2007.

[66] G. Yu, X. Bu, B. Yang, Y. Li, and C. Xiang, "Differential-type GMI magnetic sensor based on longitudinal excitation," *IEEE Sensors J.*, vol. 11, no. 10, pp. 2273–2278, Oct. 2011.

[67] S. Yabukami *et al.*, "A design of highly sensitive GMI sensor," *J. Magn. Magn. Mater.*, vols. 290–291, pp. 1318–1321, Apr. 2005.

[68] P. Delooze, L. V. Panina, D. J. Mapps, K. Ueno, and H. Sano, "CoFeB-cu layered film with crossed anisotropy for asymmetrical magnetoimpedance," *IEEE Trans. Magn.*, vol. 39, no. 5, pp. 3307–3309, Sep. 2003.

[69] M. Malátek, P. Ripka, and L. Kraus, "Double-core GMI current sensor," *IEEE Trans. Magn.*, vol. 41, no. 10, pp. 3703–3705, Oct. 2005.

[70] H. Hauser *et al.*, "MI effect in amorphous CoFe thin film trilayers and demonstrator packaging," in *Proc. 30th Int. Spring Seminar Electron. Technol. (ISSE)*, May 2007, pp. 281–286.

[71] M. Goktepe, Y. Ege, N. Bayri, and S. Atalay, "Non-destructive crack detection using GMI sensor," *Phys. Status Solidi (C)*, vol. 1, no. 12, pp. 3436–3439, Dec. 2004.

[72] P. D. Dimitropoulos, G. I. Stamoulis, and E. Hristoforou, "A 3-D hybrid Jiles-Atherton/Stoner–Wohlfarth magnetic hysteresis model for inductive sensors and actuators," *IEEE Sensors J.*, vol. 6, no. 3, pp. 721–736, Jun. 2006.

[73] C. Petridis, P. D. Dimitropoulos, and E. Hristoforou, "New magnetic field sensor based on combined flux-gate/Hall-effect arrangement," *IEEE Sensors J.*, vol. 9, no. 2, pp. 128–134, Feb. 2009.

[74] P. D. Dimitropoulos, J. N. Avaritsiotis, and E. Hristoforou, "A novel micro-fluxgate sensor based on the AMR effect of ferromagnetic film-resistors," *Sens. Actuators A, Phys.*, vol. 107, no. 3, pp. 238–247, Nov. 2003.

[75] N. Hadjigeorgiou, C. Konstantopoulos, and D. Masxas, "Fourier analysis for orthogonal and parallel fluxgate," *Key Eng. Mater.*, vol. 644, pp. 270–273, May 2015.

[76] A. Plotkin, E. Paperno, A. Samohin, and I. Sasada, "Compensation of the thermal drift in the sensitivity of fundamental-mode orthogonal fluxgates," *J. Appl. Phys.*, vol. 99, no. 8, Apr. 2006, Art. no. 08B305.

[77] I. Sasada, "Orthogonal fluxgate mechanism operated with DC biased excitation," *J. Appl. Phys.*, vol. 91, no. 10, p. 7789, 2002.

[78] M. Butta and I. Sasada, "Noise correlation in fundamental mode orthogonal fluxgate," *J. Appl. Phys.*, vol. 111, no. 7, Apr. 2012, Art. no. 07E517.

[79] P. D. Dimitropoulos, J. N. Avaritsiotis, and E. Hristoforou, "Boosting the performance of miniature fluxgates with novel signal extraction techniques," *Sens. Actuators A, Phys.*, vol. 90, nos. 1–2, pp. 56–72, May 2001.

[80] E. Paperno, "Suppression of magnetic noise in the fundamental-mode orthogonal fluxgate," *Sens. Actuators A, Phys.*, vol. 116, no. 3, pp. 405–409, Oct. 2004.

[81] P. Ripka, "New directions in fluxgate sensors," *J. Magn. Magn. Mater.*, vols. 215–216, pp. 735–739, Jun. 2000.

[82] C. Carr *et al.*, "The double star magnetic field investigation: Instrument design, performance and highlights of the first year's observations," *Annales Geophysicae*, vol. 23, no. 8, pp. 2713–2732, Nov. 2005.

[83] D. Jiles, *Introduction to Magnetism and Magnetic Materials*. Boca Raton, FL, USA: CRC Press, 2015.

[84] D. J. Griffiths, *Introduction to Electrodynamics*, 4th ed. London, U.K.: Pearson, 2013.

[85] Schlumberger. (Jul. 2020). *BF-10 Magnetic Field Induction Sensor*. [Online]. Available: https://www.slb.com/

[86] M. H. Levitt, *Spin Dynamics: Basics of Nuclear Magnetic Resonance*, 2nd ed. West Sussex, U.K.: Wiley, 2008.

[87] S. V. Kusminskiy, *Quantum Magnetism, Spin Waves, and Optical Cavities* (Springer Briefs in Physics). Cham, Switzerland: Springer, 2019.

[88] M. Schmelz *et al.*, "Thin-film-based ultralow noise SQUID magnetometer," *IEEE Trans. Appl. Supercond.*, vol. 26, no. 5, pp. 1–5, Aug. 2016.

[89] A. N. Matlashov, V. K. Semenov, and W. H. Anderson, "AC defluxing of SQUIDs," *IEEE Trans. Appl. Supercond.*, vol. 27, no. 4, pp. 1–5, Jun. 2017.

[90] Y. W. Zhou, H. Li, E. Y. Cho, H. Cai, G. Covert, and S. A. Cybart, "Electronic feedback system for superconducting quantum interference devices," *IEEE Trans. Appl. Supercond.*, vol. 30, no. 7, pp. 1–5, Oct. 2020.

[91] Z. Song *et al.*, "Noise compensation of a mobile LTS SQUID planar gradiometer for aeromagnetic detection," *IEEE Trans. Appl. Supercond.*, vol. 29, no. 8, pp. 1–5, Dec. 2019.

[92] M. Suleiman, E. G. D. Torre, and Y. Ivry, "Flexible amorphous superconducting materials and quantum devices with unexpected tunability," 2020, *arXiv:2002.10297*. [Online]. Available: https://arxiv.org/abs/2002.10297

[93] M. R. Beaumont *et al.*, "Reproducible nanostructuration of the superconducting κ-(BEDT-TTF)$_2$Cu(NCS)$_2$ phase," *Synth. Met.*, vol. 261, Mar. 2020, Art. no. 116310, [Online]. Available: http://www.sciencedirect.com/science/article/pii/S0379677919308379

[94] N. Terauchi, S. Noguchi, and H. Igarashi, "Numerical simulation of DC SQUID taking into account quantum characteristic of josephson junction," *IEEE Trans. Magn.*, vol. 51, no. 3, pp. 1–4, Mar. 2015.

[95] F. Grilli *et al.*, "Electromagnetic modeling of superconductors with commercial software: Possibilities with two vector potential-based formulations," *IEEE Trans. Appl. Supercond.*, vol. 31, no. 1, pp. 1–9, Jan. 2021.

[96] E. V. Burmistrov, V. Y. Slobodchikov, V. V. Khanin, Y. V. Maslennikov, and O. V. Snigirev, "DC SQUID modulation electronics for operation with HTS DC SQUID magnetometers in the unshielded environment," *IEEE Trans. Appl. Supercond.*, vol. 19, no. 3, pp. 206–209, Jun. 2009.

[97] *Low Field High Precision Linear 1 and 2-Axis Analog Magnetic Sensors*. [Online]. Available: https://aerospace.honeywell.com/en/learn/products/sensors/low-field-high-precision-linear-1-and-2-axis-analog-magnetic-sen

[98] RoHS SOIC. *AAL002-02E: 1.5 mT Sat. Analog Sensor, 5.5 KOhm*. [Online]. Available: https://www.nve.com/webstore/catalog/product_info.php?products_id=511

[99] AEC Sensors. *TMR2309 Datasheet*. [Online]. Available: https://www.aecsensors.com/components/com_virtuemart/shop_image/product/Magnetic-Tunnelling-Magnetoresistive-(TMR)-Linear-Sensors/pdfs/TMR2309-Datasheet-EN-V1.0a.pdf

[100] *AMI306R 3-Axis Compass*. [Online]. Available: https://www.aichi-mi.com/e-home-new/electronic-compass/ami306r-3-axis-compass/

[101] Honeywell. *SS94A*. [Online]. Available: https://media.digikey.com/pdf/Data%20Sheets/Honeywell%20Sensing%20&%20Control%20PDFs/ss94a.pdf

[102] (Apr. 2020). *Bartington Mag628/629/669*. [Online]. Available: https://www.bartington.com/mag628-629-669/

[103] *LEMI-152*. [Online]. Available: http://lemisensors.com/?p=464

[104] A. Chwala *et al.*, "Noise characterization of highly sensitive SQUID magnetometer systems in unshielded environments," *Superconductor Sci. Technol.*, vol. 26, no. 3, Feb. 2013, Art. no. 035017, doi: 10.1088%2F0953-2048%2F26%2F3%2F035017.

[105] K. Papafotis and P. P. Sotiriadis, "MAG.I.C.AL.—A unified methodology for magnetic and inertial sensors calibration and alignment," *IEEE Sensors J.*, vol. 19, no. 18, pp. 8241–8251, Sep. 2019.

[106] K. Papafotis and P. P. Sotiriadis, "Accelerometer and magnetometer joint calibration and axes alignment," *Technologies*, vol. 8, no. 1, p. 11, Jan. 2020.

[107] J. F. Vasconcelos, G. Elkaim, C. Silvestre, P. Oliveira, and B. Cardeira, "Geometric approach to strapdown magnetometer calibration in sensor frame," *IEEE Trans. Aerosp. Electron. Syst.*, vol. 47, no. 2, pp. 1293–1306, Apr. 2011.

[108] N. Ammann, A. Derksen, and C. Heck, "A novel magnetometer-accelerometer calibration based on a least squares approach," in *Proc. Int. Conf. Unmanned Aircr. Syst. (ICUAS)*, Jun. 2015, pp. 577–585.

[109] M. Kok, J. D. Hol, T. B. Schön, F. Gustafsson, and H. Luinge, "Calibration of a magnetometer in combination with inertial sensors," in *Proc. 15th Int. Conf. Inf. Fusion*, Jul. 2012, pp. 787–793.

[110] J. Metge, R. Mégret, A. Giremus, Y. Berthoumieu, and T. Décamps, "Calibration of an inertial-magnetic measurement unit without external equipment, in the presence of dynamic magnetic disturbances," *Meas. Sci. Technol.*, vol. 25, no. 12, Dec. 2014, Art. no. 125106.

[111] M. V. Gheorghe, "Calibration for tilt-compensated electronic compasses with alignment between the magnetometer and accelerometer sensor reference frames," in *Proc. IEEE Int. Instrum. Meas. Technol. Conf. (I2MTC)*, May 2017, pp. 1–6.

[112] K. Papafotis and P. P. Sotiriadis, "Computationally efficient calibration algorithm for three-axis accelerometer and magnetometer," in *Proc. 8th Int. Conf. Modern Circuits Syst. Technol. (MOCAST)*, May 2019, pp. 1–4.

[113] Y. Wu and W. Shi, "On calibration of three-axis magnetometer," *IEEE Sensors J.*, vol. 15, no. 11, pp. 6424–6431, Nov. 2015.

[114] R. Alonso and M. D. Shuster, "TWOSTEP: A fast robust algorithm for attitude-independent magnetometer-bias determination," *J. Astron. Sci.*, vol. 50, no. 4, pp. 433–451, Dec. 2002.

[115] J. M. G. Merayo, P. Brauer, F. Primdahl, J. R. Petersen, and O. V. Nielsen, "Scalar calibration of vector magnetometers," *Meas. Sci. Technol.*, vol. 11, no. 2, pp. 120–132, Jan. 2000, doi: 10.1088%2F0957-0233%2F11%2F2%2F304.

[116] K. Papafotis and P. P. Sotiriadis, "Multiple accelerometers and magnetometers joint calibration and alignment," *IEEE Sensors Lett.*, vol. 4, no. 3, pp. 1–4, Mar. 2020.

[117] E. Dorveaux, D. Vissière, A.-P. Martin, and N. Petit, "Iterative calibration method for inertial and magnetic sensors," in *Proc. 48h IEEE Conf. Decis. Control (CDC), 28th Chin. Control Conf.*, Dec. 2009, pp. 8296–8303.

[118] Y. Wu, D. Zou, P. Liu, and W. Yu, "Dynamic magnetometer calibration and alignment to inertial sensors by Kalman filtering," *IEEE Trans. Control Syst. Technol.*, vol. 26, no. 2, pp. 716–723, Mar. 2018.

[119] M. Kok and T. B. Schön, "Maximum likelihood calibration of a magnetometer using inertial sensors," in *Proc. IFAC Volumes*, 2014, vol. 47, no. 3, pp. 92–97.

[120] M. Zhu, Y. Wu, and W. Yu, "An efficient method for gyroscope-aided full magnetometer calibration," *IEEE Sensors J.*, vol. 19, no. 15, pp. 6355–6361, Aug. 2019.

[121] X. Li and Z. Li, "A new calibration method for tri-axial field sensors in strap-down navigation systems," *Meas. Sci. Technol.*, vol. 23, no. 10, Sep. 2012, Art. no. 105105.

[122] K. Papafotis and P. P. Sotiriadis, "A fast and accurate accelerometer and magnetometer alignment algorithm," *IEEE Sensors J.*, vol. 20, no. 24, pp. 15061–15067, Dec. 2020.

[123] P. P. Sotiriadis and K. Papafotis, "A single-step method for accelerometer and magnetometer axes alignment," *IEEE Trans. Instrum. Meas.*, vol. 70, pp. 1–7, 2021.

[124] P. Brown *et al.*, "Corrigendum: Magnetoresistive magnetometer for space science applications," *Meas. Sci. Technol.*, vol. 23, no. 5, Apr. 2012, Art. no. 059501.

[125] A. Zambrano and H. G. Kerkhoff, "A dependable AMR sensor system for automotive applications," in *Proc. Int. Test Conf. Asia (ITC-Asia)*, Sep. 2017, pp. 59–64.

[126] A. Bernieri, L. Ferrigno, M. Laracca, and A. Rasile, "An AMR-based three-phase current sensor for smart grid applications," *IEEE Sensors J.*, vol. 17, no. 23, pp. 7704–7712, Dec. 2017.

[127] J. M. Daughton, "GMR and SDT sensor applications," *IEEE Trans. Magn.*, vol. 36, no. 5, pp. 2773–2778, 2000.

[128] G. Rieger, K. Ludwig, J. Hauch, and W. Clemens, "GMR sensors for contactless position detection," *Sens. Actuators A, Phys.*, vol. 91, nos. 1–2, pp. 7–11, Jun. 2001.

[129] C.-C. Huang, C.-L. Lin, J.-J. Kao, J.-J. Chang, and G.-J. Sheu, "Vehicle parking guidance for wireless charge using GMR sensors," *IEEE Trans. Veh. Technol.*, vol. 67, no. 8, pp. 6882–6894, Aug. 2018.

[130] Z. Qian, D. Wang, J. M. Daughton, M. Tondra, C. Nordman, and A. Popple, "Linear spin-valve bridge sensing devices," *IEEE Trans. Magn.*, vol. 40, no. 4, pp. 2643–2645, Jul. 2004.

[131] *Triaxis 3D Joystick Position Sensor IC*. [Online]. Available: https://www.melexis.com/en/product/MLX90333/Triaxis-Absolute-3D-Joystick-Position-Sensor

[132] F. Caricchi, F. G. Capponi, F. Crescimbini, and L. Solero, "Sinusoidal brushless drive with low-cost linear Hall effect position sensors," in *Proc. IEEE 32nd Annu. Power Electron. Specialists Conf.*, vol. 2, Jun. 2001, pp. 799–804.

[133] R. S. Popovic, *Hall Effect Devices*. Bristol Philadelphia: Institute of Physics Publishing, 2004.

[134] A. Mahdi, L. Panina, and D. Mapps, "Some new horizons in magnetic sensing: high-T_c SQUIDs, GMR and GMI materials," *Sens. Actuators A, Phys.*, vol. 105, no. 3, pp. 271–285, 2003.

[135] (Jun. 2020). *Bartington Mag-13*. [Online]. Available: https://www.bartington.com/mag-13/

[136] (Sep. 2020). *Mag690*. [Online]. Available: https://www.bartington.com/mag690/

[137] P. Ripka and M. Janosek, "Advances in magnetic field sensors," *IEEE Sensors J.*, vol. 10, pp. 1108–1116, Jul. 2010.

[138] D. Ciudad, M. Díaz-Michelena, L. Pérez, and C. Aroca, "Small fluxgate magnetometers: Development and future trends in spain," *Sensors*, vol. 10, pp. 1859–1870, Mar. 2010.

[139] P. M. Drljaća, P. Kejik, F. Vincent, D. Piguet, F. Gueissaz, and R. S. Popović, "Single core fully integrated CMOS micro-fluxgate magnetometer," *Sens. Actuators A, Phys.*, vol. 110, nos. 1–3, pp. 236–241, Feb. 2004.

[140] (Jul. 2020). *Landmine UXO Detection Brochure*. [Online]. Available: https://pdf.directindustry.com/pdf/foerster-instruments/landmine-uxo-detection-brochure/16605-113277.html

[141] Schlumberger. (2015). *SURVIVOR HDS-1G*. Accessed: Aug. 2020. [Online]. Available: https://connect.slb.com/

[142] C. Siart, *Digital Geoarchaeology* (Natural Science in Archaeology), C. Siart, M. Forbriger, and O. Bubenzer, Eds. Cham, Switzerland: Springer, 2018.

[143] Schlumberger. (Jul. 2020). *DeepLook-EM*. [Online]. Available: https://www.slb.com/deeplook

[144] M. Faley *et al.*, "Magnetoencephalography using a multilayer high TC DC squid magnetometer," *Phys. Procedia*, vol. 36, pp. 66–71, Jan. 2012.

[145] *s700x Squid Magnetometer*. [Online]. Available: http://www.cryogenic.co.uk/products/s700x-squid-magnetometer

[146] Y. R. Chemla *et al.*, "Ultrasensitive magnetic biosensor for homogeneous immunoassay," *Proc. Nat. Acad. Sci. USA*, vol. 97, no. 26, pp. 14268–14272, Dec. 2000.

[147] T. Hato *et al.*, "Development of HTS-SQUID magnetometer system with high slew rate for exploration of mineral resources," *Superconductor Sci. Technol.*, vol. 26, no. 11, Sep. 2013, Art. no. 115003.

[148] C. M. Wilson *et al.*, "Observation of the dynamical Casimir effect in a superconducting circuit," *Nature*, vol. 479, no. 7373, pp. 376–379, Nov. 2011.

Neoclis Hadjigeorgiou (Graduate Student Member, IEEE) received the Diploma degree in electrical and computer engineering and the M.S. degree in mechanical engineering from the National Technical University of Athens, Greece, in 2011 and 2013, respectively, where he is currently pursuing the Ph.D. degree in the subject "Integrated Architectures for Magnetic Sensors" in electrical and computer engineering. From 2013 to 2014, he was a Research Assistant with the Laboratory of Metallurgy in Mining and Metallurgical Engineering, National Technical University of Athens. He has authored and coauthored some technical papers in IEEE conferences and some non-IEEE journals. He published a book chapter in the book *Electromagnetic Compatibility for Space Systems Design* (IGI-Global, 2018). His research interests include circuit design, magnetic sensor design, parallel programming, and GPU programming.

Konstantinos Asimakopoulos (Graduate Student Member, IEEE) completed his studies from the School of Mining and Metallurgical Engineering in 2012. He is currently pursuing the Ph.D. degree with the Department of Electrical and Computer Engineering, National Technical University of Athens (NTUA), Greece. He continued his studies with the NTUA School of Mechanical Engineering, where he completed the Interdepartmental Postgraduate Program "Automation Systems" in 2017. Since 2016, he has been a member of the Research Team with the Electronic Laboratory, Electrical and Computer Engineering School, under Prof. Paul P. Sotiriadis.

Konstantinos Papafotis (Graduate Student Member, IEEE) received the Diploma degree in electrical and computer engineering from the National Technical University of Athens, Greece, in 2015, where he is currently pursuing the Ph.D. degree, under the supervision of Prof. Paul P. Sotiriadis. He is a Teaching Assistant in several undergraduate courses and acts as an Advisor for several diploma theses. His main research interests include inertial navigation, embedded systems, and wireless sensors' systems. He is the author of several conference papers and journal articles. He has received the Best Paper Award from the IEEE International Conference on Modern Circuits and Systems Technologies in 2019. He is a regular Reviewer for many IEEE publications.

Paul P. Sotiriadis (Senior Member, IEEE) received the Diploma degree in electrical and computer engineering from the National Technical University of Athens, Greece, the M.S. degree in electrical engineering from Stanford University, Stanford, CA, USA, and the Ph.D. degree in electrical engineering and computer science from the Massachusetts Institute of Technology, Cambridge, MA, USA, in 2002.

In 2002, he joined the Department of Electrical and Computer Engineering, Johns Hopkins University, as a Faculty Member, and in 2012 he joined the Department of Electrical and Computer Engineering, National Technical University of Athens, as a Faculty Member. He is a Professor of Electrical and Computer Engineering with the National Technical University of Athens, Greece, the Director of the Electronics Laboratory with the National Technical University of Athens, and a Governing Board Member of the Hellenic Space Center, National Space Center of Greece. He runs a team of 30 researchers. He has authored and coauthored more than 160 research publications, holds one patent, and has contributed several chapters to technical books. He has led several projects in these fields funded by U.S. organizations and has collaborations with industry and national labs. His research interests include the design, optimization, and mathematical modeling of analog, mixed-signal, RF and microwave integrated and discrete circuits, sensors and instrumentation architectures, biomedical instrumentation, interconnect networks, and advanced frequency synthesis. He has been a member of technical committees of many conferences. He has received several awards, including the 2012 Guillemin-Cauer Award from the IEEE Circuits and Systems Society, the Best Paper Award from the IEEE International Symposium on Circuits and Systems in 2007, the Best Paper Award from the IEEE International Frequency Control Symposium in 2012, and the Best Paper Award from the IEEE International Conference on Modern Circuits and Systems Technology in 2019. He is an Associate Editor of the IEEE SENSORS JOURNAL. He has served as an Associate Editor for the IEEE TRANSACTIONS ON CIRCUITS AND SYSTEMS—I: REGULAR PAPERS from 2016 to 2020 and the IEEE TRANSACTIONS ON CIRCUITS AND SYSTEMS—II: EXPRESS BRIEFS from 2005 to 2010. He regularly reviews for many IEEE transactions and conferences and serves on proposal review panels.